NANO · MICRO small
www.small-journal.com

Observing Mesoscopic Nucleic Acid Capacitance Effect and Mismatch Impact via Graphene Transistors

Mingfeng Zhang, Zhibo Li, Yuan Jia, Fuquan Wang, Jinpeng Tian, Cuiping Zhang, Tingting Han, Ruiqing Xing, Weixiang Ye,* and Cheng Wang**

This work reports a molecular-scale capacitance effect of the double helical nucleic acid duplex structure for the first time. By quantitatively conducting large sample measurements of the electrostatic field effect using a type of high-accuracy graphene transistor biosensor, an unusual charge-transport behavior is observed in which the end-immobilized nucleic acid duplexes can store a part of ionization electrons like molecular capacitors, other than electric conductors. To elucidate this discovery, a cascaded capacitive network model is proposed as a novel equivalent circuit of nucleic acid duplexes, expanding the point-charge approximation model, by which the partial charge-transport observation is reasonably attributed to an electron-redistribution behavior within the capacitive network. Furthermore, it is experimentally confirmed that base-pair mismatches hinder the charge transport in double helical duplexes, and lead to directly identifiable alterations in electrostatic field effects. The bioelectronic principle of mismatch impact is also self-consistently explained by the newly proposed capacitive network model. The mesoscopic nucleic acid capacitance effect may enable a new kind of label-free nucleic acid analysis tool based on electronic transistor devices. The in situ and real-time nucleic acid detections for virus biomarkers, somatic mutations, and genome editing off-target may thus be predictable.

1. Introduction

Nucleic acids, the carriers of genetic information, control protein coding in living things and undertake diverse life behaviors. Ever since the discovery of their secondary structures, people have been making great efforts to decode the conveyed genetic ciphers for the advanced diagnosis, treatment, and therapy of diseases.[1] Pursuing these targets, precisely and reliably locating the nucleic acids with specific sequences is a fundamental mission.[2] For example, in the recent pandemic of severe acute respiratory syndrome coronavirus 2 (SARS-CoV-2), efficiently detecting target RNA fragments and base mutations is of significant importance.[3] In another area, the genome-editing technique based on the clustered regularly interspaced short palindromic repeats (CRISPR)/CRISPR-associated protein (Cas) systems is confronted with a critical off-target challenge.[4] To prevent nucleic-acid-editing failures and potential disasters,[5] developing a facile detection tool for the timely monitoring of base-editing outcomes, instead of the complete sequencing, would be worthwhile.

Based on the Watson–Crick base-pairing rules, the complementary or partial hybridization between nucleotide single strands enables the selective identification of target sequences.[6] However, the existing detection techniques are usually limited by the lack of signal generation strategies for discernible outputs. The commonly utilized nucleotide labeling typically reduces the detection instantaneity.[7] For this reason, novel label-free methods exploiting the intrinsic properties of nucleic acids, instead of extrinsic labels, are

M. Zhang, Z. Li, F. Wang, C. Zhang, T. Han, R. Xing, C. Wang
Tianjin Key Laboratory of Wireless Mobile Communications and Power Transmission
College of Electronic and Communication Engineering
Tianjin Normal University
Tianjin 300387, China
E-mail: cwang@tjnu.edu.cn

Y. Jia, J. Tian
Industrialization Center of Micro & Nano ICs and Devices
Sino-German College of Intelligent Manufacturing
Shenzhen Technology University
Shenzhen 518118, China
E-mail: jiayuan@sztu.edu.cn

The ORCID identification number(s) for the author(s) of this article can be found under https://doi.org/10.1002/smll.202105890.

DOI: 10.1002/smll.202105890

T. Han, R. Xing, C. Wang
Department of Intelligence Science and Technology
College of Artificial Intelligence
Tianjin Normal University
Tianjin 300387, China

W. Ye
Department of Physics
School of Science
Hainan University
Haikou 570228, China
E-mail: wxy@hainanu.edu.cn

W. Ye
Key Laboratory of Engineering Modeling and Statistical Computation of Hainan Province
School of Science
Hainan University
Haikou 570228, China

eagerly desired. Following this idea, the spontaneous ionization of nucleic acids in aqueous media can be exploited to realize label-free bioelectronic detections.[8] However, the fundamental understanding of bioelectronic signaling principles is still insufficient for establishing a universal guidance to this day.[9] For the nucleic acid molecules possessing delicate secondary structures, in particular, containing base-pair mismatches, the electronic sensor responses arising from ionization charges usually exhibit uncertain discrepancies. Although existing researches have attributed the cause to the structural charge distribution impact specific to the single-nucleotide polymorphism,[6,8b,10] the equivalent circuit models for describing the structural bioelectronic signaling principle are still incomplete.

In this work, we systematically investigated the bioelectronic signaling of end-immobilized nucleic acid duplexes using a type of dual-gate graphene transistor device. By exploiting the Dirac cone-shaped zero-gap bands of graphene, which allow the continuous filling of ambipolar carriers (i.e., electrons and holes),[11] we accurately quantified that the nucleic acid charges account for exciting transistor sensor signals and further discussed the base-pair mismatch impact. On the basis of the large-sample statistics, a novel phenomenological model was proposed for the first time, that is, the charge distribution in a nucleic acid duplex can be described by a capacitive network, instead of simply understood as a conductor or charged centroids.[12] Therefore, the observable transistor sensor responses induced by base-pair mismatches can be quantitatively elucidated by the charge distribution alterations relating to the molecular structures of nucleic acid duplexes and corresponding capacitive networks. Although the observation using our current graphene transistor sensors is unable to specifically locate the mismatch species and positions, the determination of mismatch existence in target strands may still be useful when embedded in the genome editing or nucleic acid diagnostic systems.[13] By timely comparing the sensor outputs with the prestored reference values (preliminarily calibrated using the fully complementary sequence), the time-efficient, in situ monitoring of anomalous pairing is potentially achievable.

2. Results and Discussion

2.1. Device and Detection Principle

To quantitatively measure the bioelectronic responses of nucleic acid duplexes, a type of biosensor, named fully solid-state graphene field-effect transistor (FSS-GFET), was used in this work (**Figure 1**). As reported in our previous work,[14] the FSS-GFET allows the tape-out of batch-made devices using standard complementary metal-oxide-semiconductor (CMOS) techniques. Under the solid-state configuration, the graphene-sensitive unit is completely encapsulated and insulated from ambient contaminants, once the device fabrication is finished. As a result, the outstanding electrical properties of fresh synthesized chemical vapor deposition (CVD) graphene can be well preserved for long-term storage and operations. Additionally, while the clean transfer of wafer-size CVD graphene is incorporated into the CMOS fabrication procedure, the device-to-device homogeneity is significantly enhanced to be comparable to that of commercial silicon transistors.[15] In this work, our GFET devices are, one time, used as disposable sensors; the device advantages in performance homogeneity and long-term stability guarantee

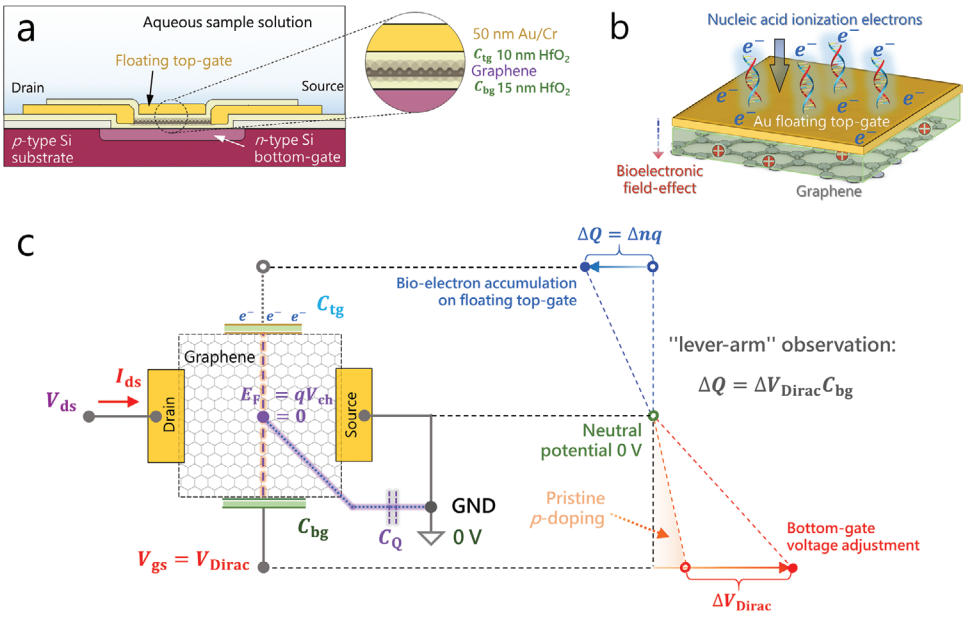

Figure 1. FSS-GFET device schematic and equivalent circuit model as a label-free electronic biosensor. a) In an FSS–GFET device, the graphene-sensing unit is encapsulated by solid HfO_2 dielectric layers, the bottom-gate electrode is made by n-type silicon via the patterned phosphorus ion implantation, complementary to the p-type silicon substrate. The floating top-gate electrode overlying graphene unit undertakes bioelectronic interactions. b) Nucleic acid duplexes are negatively charged in neutral pH aqueous media due to the ionization of phosphodiester bonds. Electrons are prone to transfer onto the top-gate electrode via gradient diffusion. c) Equivalent circuit model of an FSS-GFET biosensor. Since the graphene channel is square in this work ($W/L = 1$), the transistor conductivity is measured as $\sigma = I_{ds}/V_{ds}$.

the comparison reliability of the repetitive experiments and the validity of subsequent large-sample statistical discussion.

The sensor fabrication details are shown in Figure S1 (Supporting Information). In brief, as presented in Figure 1a, the device consists of a square-shaped graphene sheet (20 μm × 20 μm) that connects the drain and source electrodes (5 nm/45 nm Cr/Au) and creates the transistor channel. Two layers of high-κ solid dielectric HfO_2 (15 and 10 nm) encapsulate the graphene channel from the bottom and top sides, respectively. Thereby, a dual-gate transistor structure is built to allow the electric field-effect adjustments concurrently from both the bottom-gate and the floating top-gate electrodes. In particular, the floating top-gate electrode (5 nm/45 nm Cr/Au) is designed to undertake the nucleic acid interactions and enable the bioelectronic sensing. The nucleic acid molecules are assembled onto the gold surface exploiting the amino coupling with mercaptophenyl linker molecules, as shown in Figure 1b (see also Figure S2 in the Supporting Information for biochemical functionalization protocol). As the phenyl linker possesses the electronic delocalization capability,[16] the nucleic acid ionization electrons can pass through the amide bond and diffuse onto the top-gate electrode until the electric field equilibrium is achieved between both sides of the linker. The transported electrons apply electric field effect to the graphene channel via the top-gate capacitance C_{tg} (10 nm HfO_2). Thus, opposite carriers (holes) are gathered in graphene with the density variation same to that of the electrons accumulated on the floating top gate, which can be further quantified by measuring the changes of GFET conductivity σ. Compared to the conventional GFET sensors, in which biomolecules are usually anchored on the graphene surface via nonconductive alkyl linkers and confining biocharges to apply electric field in situ,[17] our FSS-GFET devices adopt the floating top-gate structure to undertake the biocharges transporting from nucleic acids. Without electric field detained on the linker molecules, the biocharge-transporting behaviors are directly related to the quantifiable electric field-effect alterations from the top gate. This distinction may enable the quantitative analysis of more informative electronic characteristics inside the biomolecules, in additional to merely the overall charge amount of nucleic acids.

As the equivalent circuit shown in Figure 1c, the dual-gate structure allows the compensation between top-gate- and bottom-gate-induced carriers. Because of the continuity of zero-gap graphene energy bands, a properly adjusted positive voltage $V_{gs} = V_{Dirac}$ applied through the bottom-gate capacitance C_{bg} depletes the holes in graphene.[18] At this time, the graphene Fermi level is adjusted to the Dirac point, at which the neutral potential ($V_{ch} = E_F/q = 0$ V) minimizes the GFET conductivity σ on the transfer characteristic curve (σ vs V_{gs}) and eliminates the impact of quantum capacitance C_Q. Thus, the shift of minimal conductivity identifier enables a "lever-arm" quantitation of the top-gate charge accumulation,[14,18b] as the offsetting relationship presented in Figure 1c. In the absence of nucleic acid duplexes, the top-gate electrode lacking of nucleic acid electrons performs a neutral potential (blue circle). Meanwhile, the bottom-gate voltage adjustment V_{gs} only has to compensate a few pristine impurity holes, and exhibits a slightly positive V_{Dirac} (red circle). Then, the presence of nucleic acid molecules on the top-gate leads to the accumulation of ionization electrons (blue dot), thus, makes V_{Dirac} perform a right shift (red dot), indicating the compensation of bioelectronic field effect from a more positive V_{gs}. Since the constant neutral graphene potential renders a linear relation between the Dirac voltage shift ΔV_{Dirac} and the effective nucleic acid charge accumulation on the top gate, the variation of accumulated charges ΔQ (or the corresponding electron density Δn) is quantified as follows

$$\Delta n = \frac{\Delta Q}{q} = \frac{\Delta V_{Dirac} C_{bg}}{q} \quad (1)$$

where $q \approx 1.602 \times 10^{-19}$ C is the elementary charge constant, and $C_{bg} \approx 944$ nF cm^{-2} is the bottom-gate capacitance (per unit area) achieved by 15 nm HfO_2.

2.2. Experimental Section

In this work, a 20-mer RNA sequence from CRISPR/Cas systems, 3′-UUC GCG UUC UUC UUU AGU UG-5′, was chosen as a template for the design of nucleic acid duplexes.[19] Without interest in genetic engineering, we focused on their bioelectronic signaling and electron transport capability. By directly functionalizing an amino group at the 3′ end without any spacer (e.g., C6-straight chain), and truncating a few nucleotides from the 5′ end,[19] we customized five RNA sequences with the various length *k*-mer (k = 12, 14, 16, 18, and 20; see Table S1 in the Supporting Information for sequences). By using the mercaptobenzoic acid *N*-hydroxysuccinimide ester (MBA-NHS) linker, the RNA sequences can be immobilized on the gold floating top-gate electrode of FSS-GFET.[14] Corresponding to the *k*-mer RNA sequences with various lengths, 32 different DNA single strands (5 complementary and 27 mismatch contained) were further designed and synthesized to form the stable RNA–DNA hybrid duplexes (see Table S2 in the Supporting Information for sequences), and the one-end immobilization of hybrid duplexes (Figure 1b) for electrical test experiments.

To systematically investigate the nucleic acid responses and base-pair mismatch impacts while ensuring the reproducibility and statistical reliability, the batch-made GFET devices were used disposably in the grouped experiments for detecting various nucleic acid duplexes (168 devices used in total). Herein, the electrical test experiments for five groups of complementary duplexes were repeated 12 times (5 × 12 = 60 devices). Similarly, the tests of mismatch-contained duplexes were divided into 27 groups, 4 repetitions for each group (27 × 4 = 108 devices). For each device, the nucleic acid immobilization was realized by incubating in the corresponding high-concentration solution of prehybridized RNA–DNA duplex (≈1×10^{-6} M; see Figure S2 in the Supporting Information for detailed protocol). The rapid saturation of irreversible amino-coupling reaction may achieve a uniform duplex site density of all the GFET devices, thus ensuring the device-to-device comparability of bioelectronic responses. The detailed device numbering rules corresponding to various duplexes are provided in Table S2 (Supporting Information).

In each electrical test experiment of a RNA–DNA duplex, the transfer characteristic curve (σ vs V_{gs}) of a GFET device was scanned twice before and after the duplex assembly to determine the curve shift ΔV_{Dirac} (see Figure S2 in the Supporting Information for operation protocol), which was then used for further fundamental discussion. All the experiments were carried out in a physiological 1 × phosphate-buffered saline (PBS, ionic strength $I \approx 150 \times 10^{-3}$ M, pH 7.2) solution.

2.3. Complementary Duplexes

Before taking base-pair mismatches into account, five groups of fully complementary duplexes were first tested, and the representative result plots are shown in **Figure 2**a–e. The values of ΔV_{Dirac} measured from k-pair duplexes (k = 12, 14, 16, 18, and 20) clearly illustrate a monotonically upturn trend with respect to the increase of duplex length k. Since the complete ionization of phosphodiester bonds in the nearly neutral pH solution, the amount of ionization electrons is linearly proportional to the duplex length k. These results are in agreement with our institution that the longer duplex brings more ionization electrons.

However, by further analyzing the complete experimental results repeated by 60 devices (see dataset in Figures S3–S7 in the Supporting Information), the transfer characteristic responses (cross labels in Figure 2f) statistically exhibit an asymptotical saturation uptrend (ΔV_{Dirac} vs k), other than a linear relation. As Equation (1) defines a proportional relation $\Delta n \propto \Delta V_{Dirac}$, the increasing trend of transported electron density Δn versus k is also nonlinear. This result suggests an anomalous electron transport property of the duplexes, unlike a regular conductor. We consider that a k-pair duplex molecule

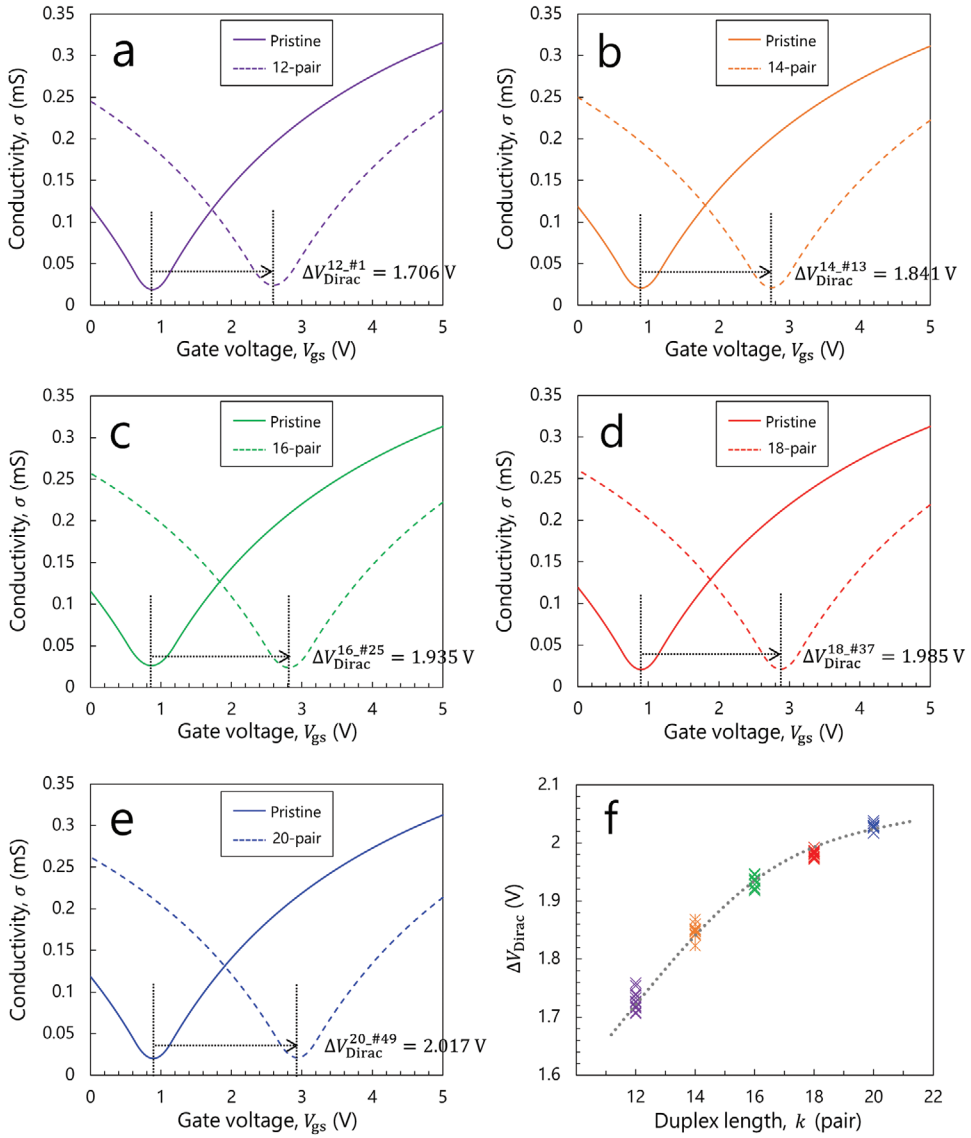

Figure 2. GFET transfer characteristic responses and statistics of complementary nucleic acid duplexes. a–e) Representative ΔV_{Dirac} responses of k-pair complementary duplexes (k = 12, 14, 16, 18, and 20). f) The complete ΔV_{Dirac} responses indicate a nonlinear positive uptrend along with the increase of base-pair number k.

brings $2k$ ionization electrons, its volume $\approx k$ nm^3 (considered as a nanocylinder with the base area ≈ 3 nm^2 and height $\approx 0.33k$ nm) leads to a high electron concentration, $c \approx 2$ nm^{-3}. Further considering that a single duplex molecule effectively occupies the gate-electrode surface area of ≈ 100 nm^2 (immobilization density $n_{site} \approx 10^{12}$ cm^{-2}[20]), the corresponding mean volume of electrode system of ≈ 5000 nm^3 (metal thickness = 50 nm) with a spare electron concentration of $c = 0$ can be estimated. If the duplex molecule behaves like a conductor connected to the metal electrode via a mercaptophenyl linker allowing electron transport, the gigantic differences in system volume and electron concentration ($k \ll 5000$) may cause the spontaneous electron diffusion driven by the Coulomb repulsive force ($F \propto c^{2/3}$) until an equilibrium at $c = k/(5000 + k) \approx k/5000$ nm^{-3} is reached.[21] Since $k \ll 5000$, the ratio of ionization electrons diffusing into the top-gate electrode would be nearly 100%, which means the linear relations, $\Delta V_{Dirac} \propto \Delta n \propto k$. Obviously, this inference is contrary to our nonlinear observation in Figure 2f, which leaves us an only reasonable explanation, that is, the end-immobilized nucleic acid duplexes cannot be considered as conductors.[22] In other words, the duplex molecules per se may also store a part of ionization electrons, somewhat similar to a capacitor effect.

2.4. Mismatch-Contained Duplexes

Based on the experiments of the fully complementary nucleic acid duplexes, we further introduced a few base-pair mismatches (Table S2, Supporting Information). As the representative results presented in **Figure 3**, the duplexes containing p mismatches (p = 1, 2, and 3) perform discernable reductions in ΔV_{Dirac} responses (see complete data of 108 devices in Figures S8–S16 in the Supporting Information), respectively, in comparison with the corresponding complementary duplexes. Overall, more mismatches lead to smaller responses in ΔV_{Dirac}, but the specific nucleotide species and positions of mismatches seem not to be significantly reflected by ΔV_{Dirac} variations.

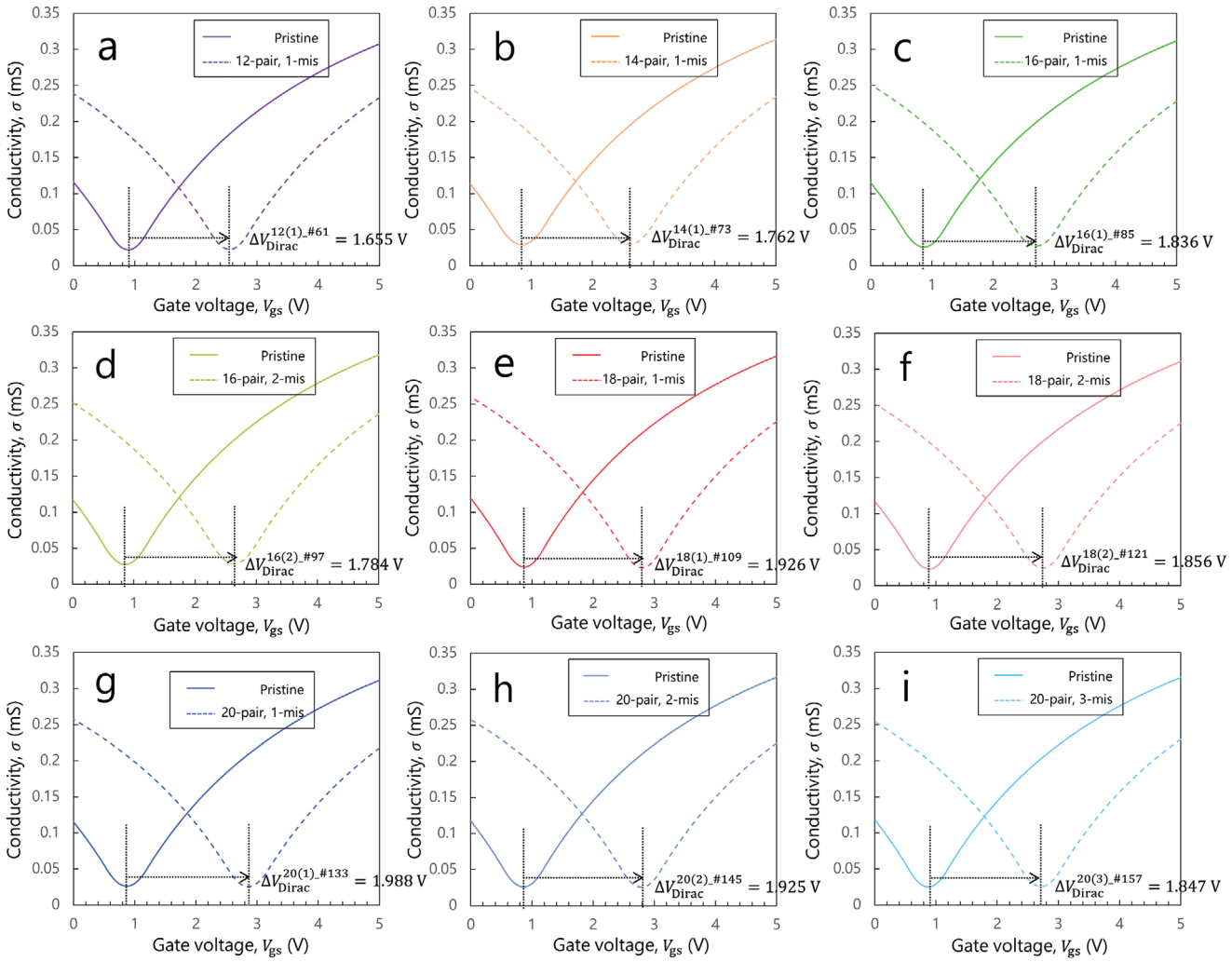

Figure 3. GFET transfer characteristic responses of mismatch-contained nucleic acid duplexes. Representative transfer characteristic curve shifts from a) 12-pair duplex with 1-mismatch, b) 14-pair duplex with 1-mismatch, c,d) 16-pair duplexes with 1- and 2-mismatch, e,f) 18-pair duplexes with 1- and 2-mismatch, g–i) 20-pair duplexes with 1-, 2-, and 3-mismatch are presented. ΔV_{Dirac} responses perform decreasing trends with respect to the mismatch increases.

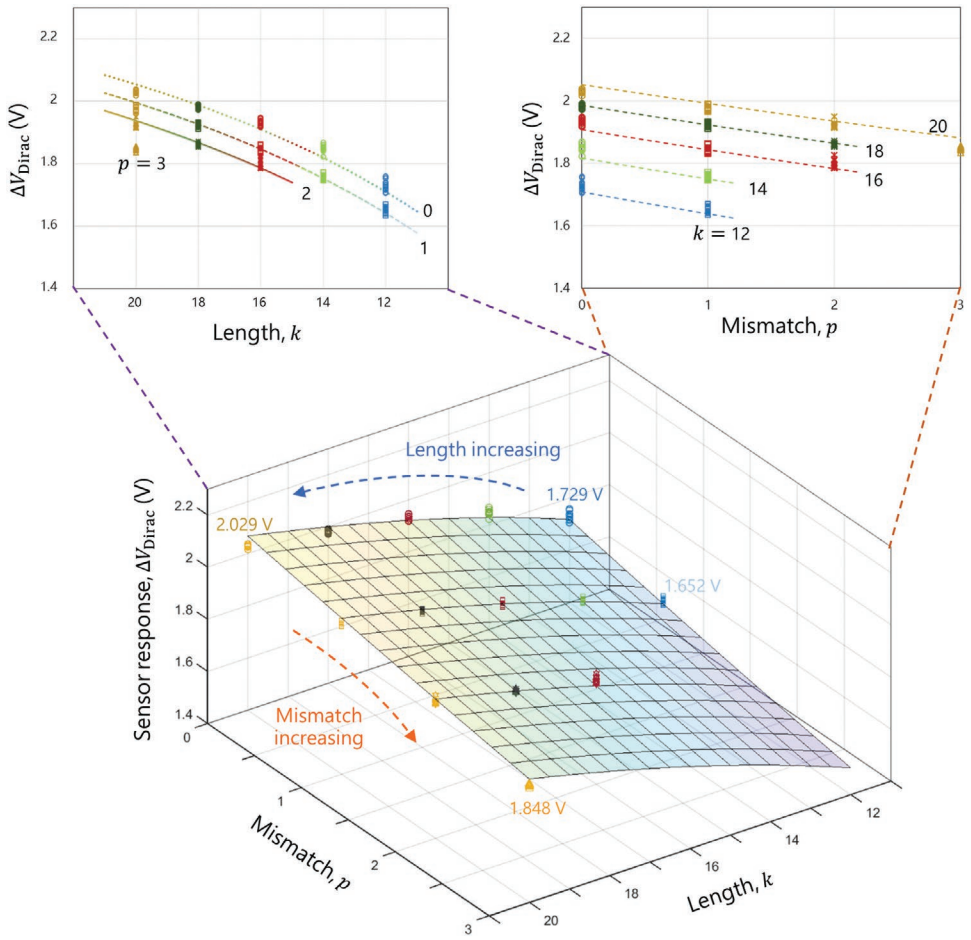

Figure 4. Statistics of GFET transfer characteristic responses. For an RNA–DNA duplex, either complementary or with the certain mismatched pairs p, the increase of duplex length k leads to the asymptotical saturation uptrend in ΔV_{Dirac} responses. For a duplex with the constant length k, the increase of mismatch amount p monotonically reduces ΔV_{Dirac}.

By summarizing all results of the complementary and mismatch-contained duplexes, the variations of ΔV_{Dirac} are plotted in the 3D rectangular coordinates, with respect to the duplex length k, and the mismatched pair number p (**Figure 4**). Since the nucleic acid duplexes with the same length possess constant ionization electrons, regardless of the number of mismatched pairs, the consistent reducing trends of ΔV_{Dirac} in Figure 4 suggest that the base-pairing states can alter the nucleic acid electron transport, and excite distinguishable ΔV_{Dirac} alterations.

2.5. Theoretical Elucidation and Modeling

In order to elucidate the nonlinear GFET experimental results, and the base-pair mismatch induced sensor response alterations, we propose a novel equivalent circuit model to quantitatively describe the bioelectronic signaling mechanism. First, we return to the equivalent circuit model of our GFET biosensor, which is illustrated in Figure 1c.[14] Since all the experimental results in this work were performed using the bottom-gate voltage adjustment $V_{gs} = V_{Dirac}$, which preserved the neutral potential of the graphene-sensitive unit, the equivalent circuit model of a nucleic acid duplex-laden GFET can be simplified to a "lever-arm" configuration, as shown in **Figure 5**a. The unchanged neutral potential of graphene ensures not only the validity of Equation (1), for the direct calculation of the effective density of top-gate-accumulated charges Δn, but also supports further discussion of the nucleic acid electron transport.

Based on the nonlinear uptrend of ΔV_{Dirac} responses plotted in Figure 2f, we expected that the nucleic acid duplex molecules possess the capacitor property. As depicted in Figure 5a, the delicate structure of one single k-pair duplex molecule assembled on the GFET is electrically modeled for the discussion of ΔV_{Dirac} response nonlinearity. Since the molecular structure of a duplex is orderly and repetitive, we choose a single nucleotide pair to define an elementary equivalent circuit unit, consisting of three capacitances (dash line box in Figure 5a). Herein, to reduce discussion complexity, the base-pairing capacitance effect is simply defined as C_P without distinguishing the species (A–U or G–C), and C_S represents the capacitance accounting for the phosphate backbone. Therefore, the equivalent circuit of a k-pair duplex can be modeled as a periodic capacitive duplex network by cascading the unit pair by pair. By further incorporating the electrical double layer (EDL) capacitances from the surrounding water solution (denoted as $C_{EDL\_*,*}$ in Figure 5a), the capacitive duplex network is connected to the top-gate capacitance C_{tg} via

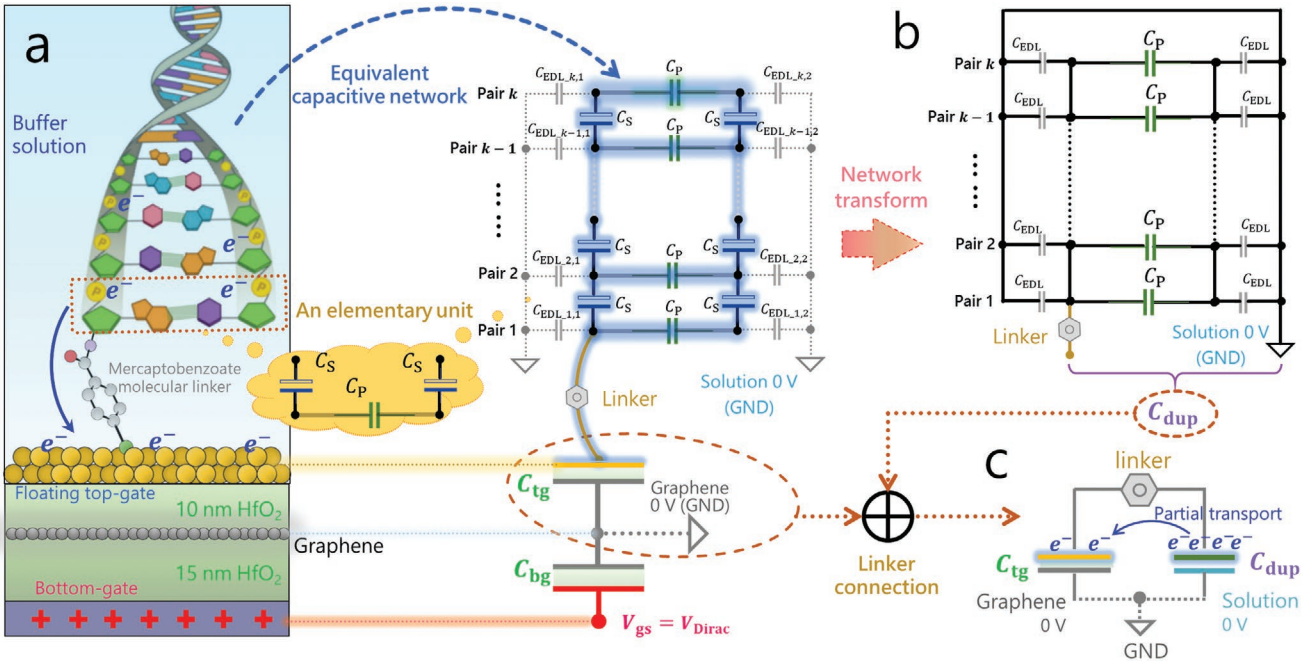

Figure 5. Electrical modeling of nucleic acid duplex signaling. a) Schematic of a duplex molecule immobilized on the floating top-gate electrode of an FSS-GFET biosensor (not to scale). Under the dual-gate electric fields adjustment, the graphene-sensing unit maintains a neutral state of carrier depletion. By modeling a base pair as an elementary capacitive unit, the *k*-pair duplex is electrically equivalent to a cascaded capacitive network, and supplies 2*k* electrons via phosphodiester bond ionization. b) By executing a continuous transform, the equivalent duplex capacitive network is simplified as a capacitance C_{dup}. c) By combining the duplex equivalent capacitance C_{dup} and the top-gate capacitance C_{tg} as a closed loop, the nonlinear uptrend of ΔV_{Dirac} responses in Figure 2f could be elucidated as a redistribution of ionization electrons between C_{dup} and C_{tg}, or effectively understood to be a partial electron transport behavior.

a conductive mercaptophenyl linker. Because of the neutral potential of graphene, which equals the common reference ground (GND) potential (water solution GND, V_{ref} = 0 V), the entire capacitive network including C_{tg} forms a closed loop. Therefore, the ionization electrons may redistribute within the entire network. This effect is equivalent to a partial transport of ionization electrons on the top-gate electrode (upper plate of C_{tg} in Figure 5a). Here, the authors would like to note that each capacitance modeled in Figure 5a may theoretically contain the parasitic conductance effect in parallel,[23] other than an ideal open circuit (infinitesimal conductance) thoroughly avoids discharge current. However, on the basis of our experimental observation, the identifiable capacitor property suggests that the parallel conductance would be small enough, only by which the persistent ionization can maintain the electrons on capacitance against the current leakage. Although the conductance of nucleic acids remains debated with no undisputed model accepted to this day,[24] for the specific case of RNA–DNA duplexes in this work, we neglect the parasitic conductance effect in the following discussion.

Technically, the entire capacitive network that we constructed in Figure 5a already enables the quantitative bioelectronic analysis of our experimental results (Figures 2–4). However, too many variables $C_{EDL\_*,*}$ in the network make the accurate numerical calculations impossible. In view of this, we use an approximation to further simplify the capacitive network. According to the Gouy–Chapman–Stern theory,[25] the EDL capacitance consists of an unchanged Helmholtz layer capacitance and a varying diffuse capacitance in series $C_{EDL} = C_{Helm}//C_{diff} = C_{Helm}\,C_{diff}/(C_{Helm} + C_{diff})$. Since the value of C_{diff} is dependent on the charging state of the specific node, C_{EDL} is theoretically not constant. However, in this work, the high ionic strength PBS solution (I = 150 × 10^{-3} M) provides the value of C_{diff} nearby the (floating gate) electrode–water interface at an approximated level of 10^6 nF cm^{-2}.[6,25a,26] In comparison, previous researches using similar biomolecule-associated interface systems have reported smaller C_{Helm} values in the order of 10^3 nF cm^{-2}.[23,26,27] Therefore, the large disparity between C_{diff} and C_{Helm} levels results in that the EDL capacitance variables $C_{EDL\_*,*}$ in Figure 5a can be regarded as a constant, which is approximately predominated by the Helmholtz layer $C_{EDL} \approx C_{Helm}$ (see Figure S17 in the Supporting Information for quantitative estimation details). By exploiting this important approximation, the capacitive network in Figure 5a becomes a highly periodic cascade of elementary capacitive grids including only three variables (C_S, C_P, and C_{EDL}), and supports the further simplification (see Figure S18 in the Supporting Information for equivalent circuit transformation details). While C_{EDL} is regarded as a constant, the network transformation indicates that the phosphate backbone capacitance C_S does not affect the charge distribution. Thus, as shown in Figure 5b, the simplified network only involves C_P and C_{EDL}. Then, the overall capacitor effect of a duplex molecule in PBS can be expressed by a combined capacitance C_{dup}, with respect to the reference ground (water solution).

Based on the discussion on the capacitance effect of nucleic acid duplex, the nonlinear ΔV_{Dirac} results that we observed in Figure 2f can be explained. As shown in Figure 5c, the entire

capacitive network combining the nucleic acid duplex capacitance C_{dup} and the top-gate capacitance C_{tg} suggests that the electrons supplied by nucleic acid ionization distribute on both C_{dup} and C_{tg} (in parallel). Thus, the ratio of top-gate-accumulated electrons (denoted as η), which effectively contributes to bioelectronic signaling, is restricted by the equation as follows

$$\eta = \frac{C_{tg}}{C_{dup} + C_{tg}} \tag{2}$$

In Equation (2), the top-gate capacitance of 10 nm HfO_2 $C_{tg} \approx$ 1.416 μF cm^{-2} is a constant. For a k-pair duplex molecule, C_{dup} is a function positively related to the duplex length k. If the duplex is fully complementary, C_{dup} is represented by a proportional function (see Figure 5b)

$$C_{dup}(k) = kC_{EDL} + k\left(C_P // C_{EDL}\right) = \frac{C_P C_{EDL} + {C_{EDL}}^2}{C_P + C_{EDL}} k \tag{3}$$

By introducing this linear relation $C_{dup} \propto k$ into Equation (2), we learn that the electron transport ratio η is negatively related to the duplex length k. As a result, along with the extension of a k-pair duplex (bring $2k$ ionization electrons), the continuous reducing $\eta(k)$ may lead to the increase trend of transported electron lower than the linear relation. This inference is in agreement with the asymptotical saturation uptrend of ΔV_{Dirac} results in Figure 2.

Furthermore, the base-pair mismatches are taken into account. While the hydrogen bonds between well-paired bases lead to the surrounding water molecules being highly polarized,[28] the effective permittivity of a base-pairing capacitance C_P (refer to Figure 5a) would be low. Then, the mismatch breaking hydrogen bonds may disorder the water molecules, thus concurrently enlarge the value of C_P via the enhancement of effective permittivity. Here, we set a new variable $C_P' > C_P$ as the mismatch capacitance to modify Equation (3). The capacitive network function describing a k-pair duplex containing p mismatches ($0 \le p < k$) is given by

$$C_{dup}(k,p) = kC_{EDL} + (k-p)\left(C_P // C_{EDL}\right) + p\left(C_P' // C_{EDL}\right) \tag{4}$$

While $p = 0$, Equation (4) degrades into Equation (3). If $p \neq 0$, the larger mismatch capacitance $C_P' > C_P$ leads to $(C_P' // C_{EDL}) > (C_P // C_{EDL})$ in Equation (4). Hence, we have $C_{dup}(k,p) > C_{dup}(k,0) = C_{dup}(k)$, which results in the lower η in Equation (2). Consequently, the mismatch-contained duplexes may store more ionization electrons than the corresponding complementary k-pair duplexes, and thus result in weaker bioelectronic responses. This conclusion supports the ΔV_{Dirac} results of mismatch-contained duplexes in Figures 3 and 4. Moreover, Equation (4) also suggests that position of mismatches cannot be specifically identified. This point provides a plausible explanation of the almost undistinguishable ΔV_{Dirac} results, which were measured from the duplexes with same k and p parameters, whereas the base-pair mismatches are not completely same (see Table S2 and Figures S8–S16 in the Supporting Information for the complete dataset).

2.6. Numerical Analysis and Quantitation

Based on the capacitive network equivalence that we proposed in Figure 5, the nonlinear increasing trend of bioelectronic responses (ΔV_{Dirac} vs k in Figure 4) and the decreasing effects from base-pair mismatches (ΔV_{Dirac} vs p in Figure 4) have been qualitatively explained. To further quantitatively extract the bioelectronic signaling parameters from the experimental results, the mesoscopic capacitive network modeling from a single duplex molecule (Figure 5a) has to be generalized to a macroscopic scale for the numerical analysis of experimental data.

We regard that the duplex molecules immobilized on the gold surface (floating top gate) may obey the even distribution. Thus, the self-assembled monolayer (SAM) consisting of duplex molecules may statistically perform the electrical parameters identical to those of the delicate single-molecule model in Figure 5. To correlate the mesoscopic models and the macroscopic experimental data, the site density of duplex-laden gold surface n_{site} is introduced. By further employing Equation (1), the effective electron ratio η can be statistically estimated as $\overline{\eta}$, based on the experimental observation of ΔV_{Dirac}

$$\overline{\eta} = \frac{\Delta n}{2kn_{site}} = \frac{C_{bg}}{2kqn_{site}} \Delta V_{Dirac} \tag{5}$$

In Equation (5), we use a typical value of the nucleic acid hybrid immobilization density on gold surface, which is previously measured as $n_{site} \approx 10^{12}$ cm^{-2}.[20] Thereby, the experimental data of ΔV_{Dirac} summarized in Figure 4 can be processed into $\overline{\eta}$ values, as plotted in the 3D rectangular coordinates (**Figure 6**). Since we regard $\overline{\eta} = \eta$, by using Equation (2), the equivalent duplex capacitance values $C_{dup}(k,p)$, and the elementary capacitance parameters C_{EDL}, C_P and C_P' can be quantified via a numerical fitting.

By introducing Equation (4) into Equation (2), the theoretical model expressed by a function of $\eta(k, p)$ with two variables $k \in$ [12, 20] and $p \in$ [0, 3] was fitted by a global regression algorithm using the $\overline{\eta}$ values calculated by Equation (5). As plotted in Figure 6, the parameter quantitation results, $C_{EDL} \approx$ 161.8 nF cm^{-2}, $C_P \approx$ 7.01 nF cm^{-2}, and $C_P' \approx$ 577.2 nF cm^{-2}, create a highly correlative fitting surface of $\eta(k, p)$. The determination coefficient $R^2 = 0.972$ demonstrates the modeling validity that the distribution of nucleic acid ionization electrons indeed can be described by the equivalent model of capacitive network (Figure 5). In particular, the authors would like to note that the capacitive network in this work is a phenomenological model describing the lumped electrical behaviors of the duplex–electrode system in high ionic strength aqueous media. Since our modeling is based on the experimental observation of the phenological bioelectronic signals, the abstracted fitting parameters may not hold clear physical meanings, strictly corresponding to the molecular scale entities. In other words, although our fitting results are basically in agreement with some experimental investigations using similar biointerface systems (e.g., interfacial capacitance, C_{EDL}),[23,26,27] the values of these parameters should not be unconditionally used as the evidence to support theoretical calculation researches, which may require more strict experimental verifications (e.g., single-molecule tests in sub-nanoscale[24b,e]). Besides, we learned that our fitting result $C_P \ll C_P'$ indicates a severe reduction of

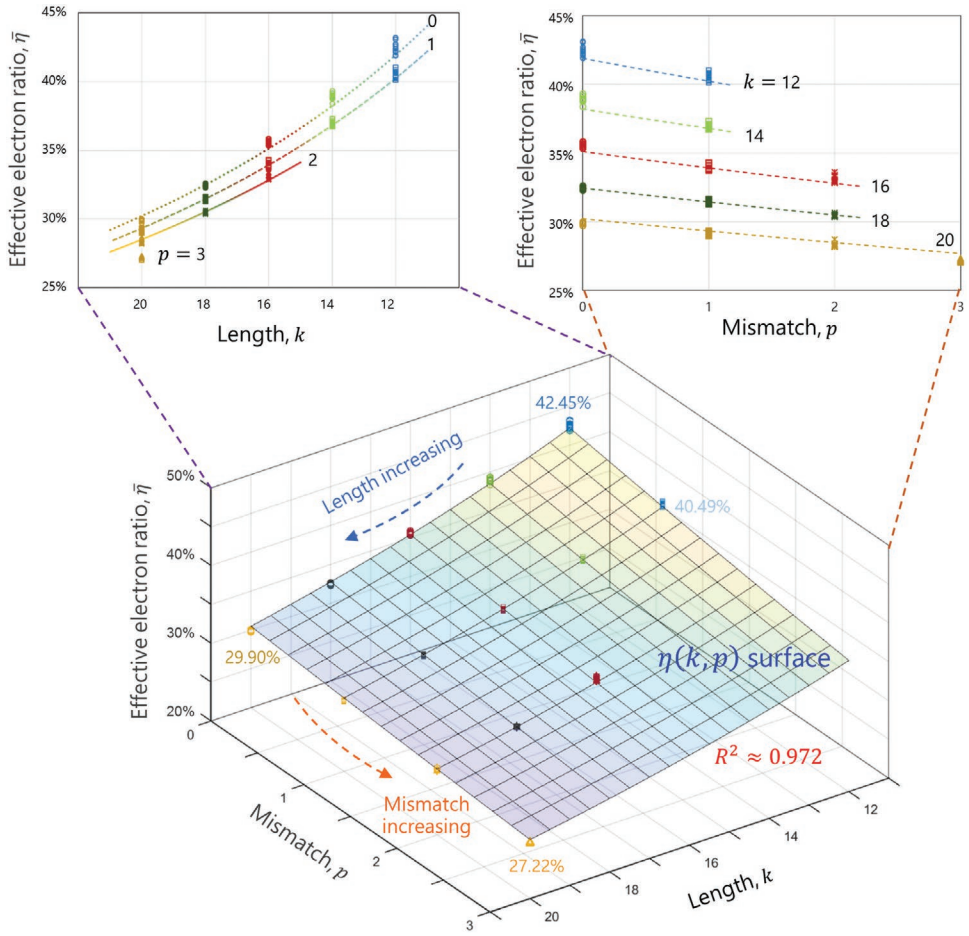

Figure 6. Effective electron ratio trends affected by the duplex length k and mismatch amount p. By using Equation (5), the macroscopically observed GFET responses (ΔV_{Dirac}) are processed into the statistical values of effective electron ratio $\bar{\eta}$. By executing numerical fitting using Equations (2) and (4), the equivalent capacitive circuit parameters of nucleic acid duplexes can be estimated.

capacitance due to the complementary base pairing. This result could be qualitatively explained by the hydrogen-bond-induced proton (hydrogen ion) tunneling effect in the highly polarized water ambience.[29] Based on this theory, the proton tunneling effectively enlarges the leakage current between the paired bases and makes the capacitance discharge easier. In other words, the leakage current reduces the electron storage capability and exhibits a much lower capacitance level.

In summary, we carried out the numerical analysis of the equivalent capacitive model for the quantitative elucidation of the bioelectronic signaling principle of nucleic acid duplexes, and the base-pair mismatch impacts. Although the electrical modeling in this work is phenomenological and includes approximations, the satisfactory statistical performances still demonstrated its validity in the quantitative analysis of nucleic acid sensing and mismatch monitoring experiments.

3. Conclusion

In conclusion, we systematically investigated the bioelectronic responses of nucleic acid duplexes using the label-free GFET biosensor devices. Based on the experimental results, the electric-field-effect signaling principle of charged nucleic acid duplexes was elucidated by a phenomenological capacitive network model proposed in this work. Importantly, this equivalent model reveals that the nucleic acid duplex molecules with one end immobilized in the vicinity of electrode–water interface possess the charge storage capability. The differences in duplex length and single nucleotide polymorphism manifest their impacts in varying the corresponding elementary capacitances, and thus change the capacitance performance of the entire network. This capacitive network modeling research may fundamentally supply rationales for the design and performance improvement of novel label-free nucleic acid biosensors, and further promote the applications of convenient electronic nucleic acid analysis tools based on transistor devices.

Supporting Information

Supporting Information is available from the Wiley Online Library or from the author.

Acknowledgements

M.Z. and Z.L. contributed equally to this work. This work was funded by the National Natural Science Foundation of China (Grant Nos. 61901300, 62104160, 62105229, and 61704122), the Aeronautical Science Foundation of China (Grant No. 2019ZD069002), and the Natural Science Foundation of Tianjin City (Grant No. 20JCYBJC00300). The authors are grateful to the technical assistance from the Funding Program of Tianjin Higher Education Creative Team and the State Key Joint Laboratory of Environmental Simulation and Pollution Control (ESPC at Tsinghua University).

Conflict of Interest

The authors declare no conflict of interest.

Data Availability Statement

The data that support the findings of this study are available from the corresponding author upon reasonable request.

Keywords

base-pair mismatches, capacitive network model, electron transport, label-free graphene transistor biosensors, nucleic acid duplexes

Received: September 26, 2021
Revised: December 5, 2021
Published online: January 24, 2022

[1] G. Segrè, *Nature* **2000**, *404*, 437.
[2] G. D. Poore, E. Kopylova, Q. Zhu, C. Carpenter, S. Fraraccio, S. Wandro, T. Kosciolek, S. Janssen, J. Metcalf, S. J. Song, J. Kanbar, S. Miller-Montgomery, R. Heaton, R. Mckay, S. P. Patel, A. D. Swaffod, R. Knight, *Nature* **2020**, *579*, 567.
[3] Z. Qin, R. Peng, I. K. Baravik, X. Liu, *Matter* **2020**, *3*, 628.
[4] Y. Fu, J. A. Foden, C. Khayter, M. L. Maeder, D. Reyon, J. K. Joung, J. D. Sander, *Nat. Biotechnol.* **2013**, *31*, 822.
[5] a) B. Wienert, S. K. Wyman, C. D. Richardson, C. D. Yeh, P. Akcakaya, M. J. Porritt, M. Morlock, J. T. Vu, K. R. Kazane, H. L. Watry, L. M. Judge, B. R. Conklin, M. Maresca, J. E. Corn, *Science* **2019**, *364*, 286; b) E. Zuo, Y. Sun, W. Wei, T. Yuan, W. Ying, H. Sun, L. Yuan, L. M. Steinmetz, Y. Li, H. Yang, *Science* **2019**, *364*, 289.
[6] S. Sorgenfrei, C.-y. Chiu, M. Johnston, C. Nuckolls, K. L. Shepard, *Nano Lett.* **2011**, *11*, 3739.
[7] a) A. Johnson-Buck, X. Su, M. D. Giraldez, M. Zhao, M. Tewari, N. G. Walter, *Nat. Biotechnol.* **2015**, *33*, 730; b) T. G. Drummond, M. G. Hill, J. K. Barton, *Nat. Biotechnol.* **2003**, *21*, 1192; c) B. Zhang, B. A. Pinsky, J. S. Ananta, S. Zhao, S. Arulkumar, H. Wan, M. K. Sahoo, J. Abeynayake, J. J. Waggoner, C. Hopes, M. Tang, H. Dai, *Nat. Med.* **2017**, *23*, 548.
[8] a) S. Sorgenfrei, C.-y. Chiu, R. L. Gonzalez Jr, Y.-J. Yu, P. Kim, C. Nuckolls, K. L. Shepard, *Nat. Nanotechnol.* **2011**, *6*, 126; b) M. T. Hwang, P. B. Landon, J. Lee, D. Choi, A. H. Mo, G. Glinsky, R. Lal, *Proc. Natl. Acad. Sci. USA* **2016**, *113*, 7088; c) N. Nakatsuka, K.-A. Yang, J. M. Abendroth, K. M. Cheung, X. Xu, H. Yang, C. Zhao, B. Zhu, Y. S. Rim, Y. Yang, *Science* **2018**, *362*, 319.
[9] a) C. Wang, Y. Li, Y. Zhu, X. Zhou, Q. Lin, M. He, *Adv. Funct. Mater.* **2016**, *26*, 7668; b) Y. Li, C. Wang, Y. Zhu, X. Zhou, Y. Xiang, M. He, S. Zeng, *Biosens. Bioelectron.* **2017**, *89*, 758; c) C. Wang, J. Kim, Y. Zhu, J. Yang, G.-H. Lee, S. Lee, J. Yu, R. Pei, G. Liu, C. Nuckolls, J. Hone, Q. Lin, *Biosens. Bioelectron.* **2015**, *71*, 222; d) Y. Li, Y. Zhu, C. Wang, M. He, Q. Lin, *Biosens. Bioelectron.* **2019**, *126*, 59.
[10] K. M. Cheung, J. M. Abendroth, N. Nakatsuka, B. Zhu, Y. Yang, A. M. Andrews, P. S. Weiss, *Nano Lett.* **2020**, *20*, 5982.
[11] L. Tarruell, D. Greif, T. Uehlinger, G. Jotzu, T. Esslinger, *Nature* **2012**, *483*, 302.
[12] C. Wang, W. Ye, Y. Li, Y. Zhu, Q. Lin, M. He, *Biosens. Bioelectron.* **2019**, *129*, 93.
[13] a) S. Balderston, J. J. Taulbee, E. Celaya, K. Fung, A. Jiao, K. Smith, R. Hajian, G. Gasiunas, S. Kutanovas, D. Kim, J. Parkinson, K. Dickerson, J.-J. Ripoll, R. Peytavi, H.-W. Lu, F. Barron, B. R. Goldsmith, P. G. Collins, I. M. Conboy, V. Siksnys, K. Aran, *Nat. Biomed. Eng.* **2021**, *5*, 713; b) R. Hajian, S. Balderston, T. Tran, T. DeBoer, J. Etienne, M. Sandhu, N. A. Wauford, J.-Y. Chung, J. Nokes, M. Athaiya, J. Paredes, R. Peytavi, B. Goldsmith, N. Murthy, I. M. Conboy, K. Aran, *Nat. Biomed. Eng.* **2019**, *3*, 427.
[14] C. Wang, J. Wu, Y. He, Z. Song, S. Shi, Y. Zhu, Y. Jia, W. Ye, *Nano Lett.* **2019**, *20*, 166.
[15] Y. Hao, M. Bharathi, L. Wang, Y. Liu, H. Chen, S. Nie, X. Wang, H. Chou, C. Tan, B. Fallahazad, H. Ramanarayan, C. W. Magnuson, E. Tutuc, B. I. Yakobson, K. F. McCarty, Y.-W. Zhang, P. Kim, J. Hone, L. Colombo, R. S. Ruoff, *Science* **2013**, *342*, 720.
[16] a) J. Heo, H. Ahn, J. Won, J. G. Son, H. K. Shon, T. G. Lee, S. W. Han, M.-H. Baik, *Science* **2020**, *370*, 214; b) L. Venkataraman, J. E. Klare, C. Nuckolls, M. S. Hybertsen, M. L. Steigerwald, *Nature* **2006**, *442*, 904; c) J. Zhu, J. McMorrow, R. Crespo-Otero, G. Ao, M. Zheng, W. P. Gillin, M. Palma, *J. Am. Chem. Soc.* **2016**, *138*, 2905.
[17] a) Y. Ohno, K. Maehashi, K. Matsumoto, *J. Am. Chem. Soc.* **2010**, *132*, 18012; b) W. Fu, L. Feng, G. Panaitov, D. Kireev, D. Mayer, A. Offenhäusser, H.-J. Krause, *Sci. Adv.* **2017**, *3*, e1701247.
[18] a) C. Wang, B. Zhang, Y. Li, X. Zhao, *IEEE Wirel. Commun.* **2020**, *27*, 44; b) Y. Huang, E. Sutter, N. N. Shi, J. Zheng, T. Yang, D. Englund, H.-J. Gao, P. Sutter, *ACS Nano* **2015**, *9*, 10612; c) Y. Zhu, C. Wang, N. Petrone, J. Yu, C. Nuckolls, J. Hone, Q. Lin, *Appl. Phys. Lett.* **2015**, *106*, 123503.
[19] M. Jinek, K. Chylinski, I. Fonfara, M. Hauer, J. A. Doudna, E. Charpentier, *Science* **2012**, *337*, 816.
[20] a) B. P. Nelson, T. E. Grimsrud, M. R. Liles, R. M. Goodman, R. M. Corn, *Anal. Chem.* **2001**, *73*, 1; b) F. Yu, D. Yao, W. Knoll, *Nucleic Acids Res.* **2004**, *32*, e75.
[21] Y. N. Kryuchkov, *Refract. Ind. Ceram.* **2001**, *42*, 390.
[22] a) A. Malyshev, *Phys. Rev. Lett.* **2007**, *98*, 096801; b) J. C. Genereux, J. K. Barton, *Chem. Rev.* **2010**, *110*, 1642; c) R. G. Endres, D. L. Cox, R. R. Singh, *Rev. Mod. Phys.* **2004**, *76*, 195.
[23] L. Wang, M. Veselinovic, L. Yang, B. J. Geiss, D. S. Dandy, T. Chen, *Biosens. Bioelectron.* **2017**, *87*, 646.
[24] a) H.-W. Fink, C. Schönenberger, *Nature* **1999**, *398*, 407; b) Y. Li, J. M. Artés, B. Demir, S. Gokce, H. M. Mohammad, M. Alangari, M. P. Anantram, E. E. Oren, J. Hihath, *Nat. Nanotechnol.* **2018**, *13*, 1167; c) R. Sha, L. Xiang, C. Liu, A. Balaeff, Y. Zhang, P. Zhang, Y. Li, D. N. Beratan, N. Tao, N. C. Seeman, *Nat. Nanotechnol.* **2018**, *13*, 316; d) J. D. Slinker, N. B. Muren, S. E. Renfrew, J. K. Barton, *Nat. Chem.* **2011**, *3*, 228; e) X. Guo, A. A. Gorodetsky, J. Hone, J. K. Barton, C. Nuckolls, *Nat. Nanotechnol.* **2008**, *3*, 163.
[25] a) W. Schmickler, *Chem. Rev.* **1996**, *96*, 3177; b) D. J. Bonthuis, S. Gekle, R. R. Netz, *Phys. Rev. Lett.* **2011**, *107*, 166102.

[26] G. Palazzo, D. De Tullio, M. Magliulo, A. Mallardi, F. Intranuovo, M. Y. Mulla, P. Favia, I. Vikholm-Lundin, L. Torsi, *Adv. Mater.* **2015**, *27*, 911.

[27] a) A. Mahadhy, E. Ståhl-Wernersson, B. Mattiasson, M. Hedström, *Biotechnol. Rep.* **2020**, *28*, e00568; b) A. Mahadhy, E. Ståhl-Wernersson, B. Mattiasson, M. Hedström, *Biotechnol. Rep.* **2014**, *3*, 42.

[28] a) M. Devereux, P. Popelier, *J. Phys. Chem. A* **2007**, *111*, 1536; b) Y. Mo, *J. Mol. Model.* **2006**, *12*, 665.

[29] a) X.-Z. Li, B. Walker, A. Michaelides, *Proc. Natl. Acad. Sci. USA* **2011**, *108*, 6369; b) A. Godbeer, J. Al-Khalili, P. Stevenson, *Phys. Chem. Chem. Phys.* **2015**, *17*, 13034; c) M. H. Lee, O. F. Sankey, *J. Phys.: Condens. Matter* **2008**, *21*, 035110.